Inverter Power Control Based on DC-Link Voltage Regulation for IPMSM Drives Without Electrolytic Capacitors

Nannan Zhao, Gaolin Wang, *Member, IEEE*, Dianguo Xu, *Fellow, IEEE*, Lianghong Zhu, Guozhu Zhang, and Junya Huo

***Abstract*—DC-link electrolytic capacitor critically affects the lifetime of the motor drive system. This paper proposes an inverter power control strategy based on dc-link voltage regulation for the electrolytic capacitor-less interior permanent magnet synchronous motor drive system. The dc-link electrolytic capacitor is replaced by a small film capacitor and the power factor correction circuit is also eliminated. Hence, the inverter power should be regulated effectively to achieve high input power factor and low grid current harmonics. The inverter power control loop based on proportional resonant (PR) controller is established to regulate the inverter power into sinusoidal wave. The PR controller can be designed to achieve a high gain at the desired frequency and the parameters are easy to design due to the simple structure. In addition, a power compensation method based on the dc-link voltage regulation is used to diminish the error of inverter power control, which does not depend on the precise calculation and is easy to realize. The effectiveness of the proposed method is demonstrated by the experimental results on an air conditioner. The input power factor can reach 0.992 and the harmonics of grid current are considerably lower than the requirement of EN61000-3-2 standard.**

***Index Terms*—DC-link voltage regulation, grid current harmonics, high-power factor, interior permanent magnet synchronous motor (IPMSM), inverter power control, small dc-link capacitor.**

I. Introduction

In RECENT years, interior permanent magnet synchronous motors (IPMSMs) have been widely used in industrial applications and home appliances [1]–[6]. Large volume electrolytic capacitors are usually utilized at the dc-link of IPMSM drive to buffer and store energy, which can stabilize the dc-link voltage and supply power for the inverter. Meanwhile, the power factor correction (PFC) circuit is necessary to improve the power factor and reduce the total harmonic distortion (THD) of the input current in fractional horsepower motor drives. However, the electrolytic capacitor containing the electrolyte results in lifetime decrease and volume increase of the drive system [7]–[14]. In order to solve these problems, the electrolytic capacitor-less ac motor drive technique has been developed [15]–[23]. Compared with the traditional drive system, the decreased capacity of the dc-link capacitor can effectively reduce the drive system volume. Because of the elimination of the PFC circuit, the efficiency and reliability of the drive system can be improved. Meanwhile, the cost of the system can also be reduced, which is an important concern in industry applications.

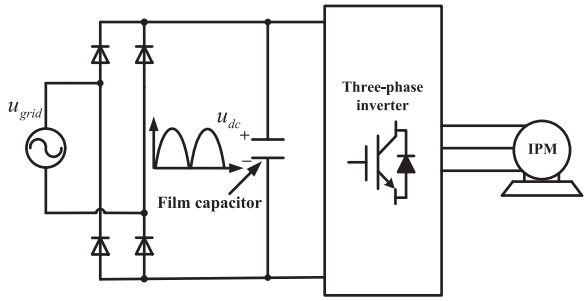

Fig. 1. Electrolytic capacitor-less IPMSM drive system.

As shown in Fig. 1, the capacity of the applied dc-link electrolytic capacitor is selected from several hundred to several thousand microfarads in the drive system using a single-phase diode rectifier for home appliances. In the electrolytic capacitor-less drive system, the capacity is usually lower than 2%–5% of the electrolytic capacitor. Due to the remarkably decreased capacity of the dc-link capacitor, the energy stored in the film capacitor is difficult to maintain dc-link voltage constant. As a result, the dc-link voltage will fluctuate with the grid voltage. However, as the constant dc-link voltage in the traditional motor drive system leads to a narrow conduction angle of the diode rectifier, the PFC circuit is required to broaden the conduction angle and reduce the current harmonics. In this way, the fluctuated dc-link voltage makes it possible to achieve high input power factor. Therefore, the PFC circuit can be eliminated

Manuscript received July 28, 2016; revised October 9, 2016 and December 13, 2016; accepted February 8, 2017. Date of publication February 17, 2017; date of current version October 6, 2017. This work was supported in part by the Research Fund for the National Science Foundation of China under Grant 51522701, in part by the Power Electronics Science and Education Development Program of Delta Environmental and Educational Foundation under Grant DREK2015002, and in part by the Natural Science Foundation of Heilongjiang Province under Grant E2016028. Recommended for publication by Associate Editor A. M. Trzynadlowski.

N. Zhao, G. Wang, and D. Xu are with the School of Electrical Engineering and Automation, Harbin Institute of Technology, Harbin 150001, China (e-mail: znn429@126.com; WGL818 @hit.edu.cn; xudiang@hit.edu.cn).

L. Zhu, G. Zhang, and J. Huo are with the GD Midea Air-Conditioning Equipment Co., Ltd., Foshan 528311, China (e-mail: zhulh@midea.com.cn; zhanggz2@midea.com.cn; huojy@midea.com.cn).

Color versions of one or more of the figures in this paper are available online at http://ieeexplore.ieee.org.

Digital Object Identifier 10.1109/TPEL.2017.2670623

to reduce the cost and improve the reliability of the drive system. Some methods to improve the input power factor have been developed under the circumstance without the PFC circuit [24]–[31]. Meanwhile, the THD of the grid current is an important concern in home appliances, which should satisfy the standard of EN61000-3-2.

There are two major solutions to deal with the mentioned issues. The first solution is to modify the circuit topology [24]–[26]. A single-phase to three-phase adjustable-speed system consisting of a diode rectifier and a single-stage boost inverter was proposed in [24]. By using the harmonic injection method, the drive system can achieve high input power factor and small dc-link voltage ripple. A dc-link shunt compensator (DSC) for the small dc-link capacitor system was applied in [25]. The DSC operating as an energy buffer compensated the power difference between the grid and the drive system. In [26], the topology consisting of a half-bridge rectifier and a four-switch three-phase inverter with two small film capacitors was presented. Additionally, the method based on the predictive control and the instantaneous power theory was proposed to shape the grid current and increase the power factor.

The other solution is to control the inverter power to improve the power factor and reduce the THD of grid current [27]–[31]. The inverter power control strategy based on the energy flow of power source was introduced in [27]. The three-phase inverter regulated the input current waveform using an additional current controller. The proposed method could improve the power factor while the THD of grid current was not mentioned. In order to reduce the THD, the sinusoidal *d*- and *q*-axis current generation was replaced by an approximately trapezoidal waveform generation in [28]. As the dc-link voltage fluctuated severely with twice the frequency of the grid voltage, a novel flux-weakening method named average voltage constraint was proposed in [29]. The average voltage represents the mean value of the fluctuated dc-link voltage, which is regarded as a constraint to generate the *d*-axis flux-weakening current. The typical values of the power factor and the THD are 0.96 and 18%, which can meet the requirements of EN61000-3-2. Furthermore, a power control loop was constructed to achieve the high-power factor, which was regulated by a proportional-integral (PI) controller and a repetitive controller. The maximum power factor was 0.987 in [30]. The direct three-phase inverter power control method was applied to improve the electrolytic capacitor-less drive performance in [31]. As the limited bandwidth of the *d*-and *q*-axis current PI controllers decreases the tracking performance of the power control loop, the direct power control can eliminate the error of the inverter power control. The inverter power reference is generated by the difference of the ideal grid input power and the film capacitor power.

In this paper, a novel inverter power control algorithm is proposed including an inverter power control loop with PR controller and a power compensation method based on dc-link voltage regulation, in order to achieve high input power factor and low grid current harmonics of the electrolytic capacitor-less drive system. The inverter power control loop with PR controller is aimed at regulating the inverter power to be sinusoidal. The PR controller is specific to the sinusoidal signals, which can achieve a high gain at the desired frequency. Meanwhile, the parameters are easy to design due to the simple structure. Compared with the existing inverter power control method strictly based on the power relationships of the drive system, an improved power compensation method based on the dc-link voltage regulation is applied to enhance the inverter power control performance. Due to the elimination of the PFC circuit in the electrolytic capacitor-less drive system, the grid input side and the inverter output side have been connected by the dc-link. Hence, the distorted inverter power can be detected by the dc-link voltage. Besides, the additional power compensation can be realized by the dc-link voltage regulation. The compensation method does not depend on the precise calculation and is easy to realize. Meanwhile, an output voltage modification method is applied to impose the output of the dc-link voltage regulation block to the voltage vector reference of the motor, which mainly considers the smallest magnitude for certain power modification.

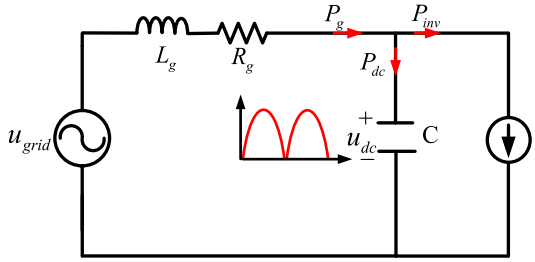

Fig. 2. Simplified block diagram of the electrolytic capacitor-less drive system.

This paper is organized as follows. Section II analyzes the power characteristics of the electrolytic capacitor-less drive system. Section III introduces the proposed inverter power control method and the scheme of the dc-link voltage regulation, including the generation of dc-link voltage reference, and the effect of the fluctuated dc-link voltage on the drive system. The experimental results prove the validity of the proposed method in Section IV.

II. Analysis of Electrolytic Capacitor-Less Drive System to Achieve High Power Factor

A. Grid Input Power of the Drive System

Fig. 2 shows the simplified block diagram of the electrolytic capacitor-less motor drive system. The grid voltage $u_{\rm grid}$ can be presented as follows:

$$u_{\rm grid} = U_g \sin\left(\omega_g t + \varphi_g\right) \tag{1}$$

where U_g, ω_g, and φ_g denote the peak amplitude, the angular velocity, and the initial phase of the grid voltage, respectively.

In order to achieve the unity power factor, the phase of the grid current $i_{\rm grid}$ should be synchronous with the grid voltage. So the expected grid input power P_g can be calculated as

$$P_g = u_{\rm grid} i_{\rm grid} = U_g I_g \sin^2\left(\omega_g t + \varphi_g\right) \tag{2}$$

where I_g is the amplitude of the grid current.

B. Power Characteristics of the Electrolytic Capacitor-Less Drive System

The grid input power of the drive system P_g can be divided into two parts: the film capacitor power $P_{\rm dc}$ and the three-phase inverter power $P_{\rm inv}$, which can be expressed as

$$P_g = P_{\rm dc} + P_{\rm inv}. \tag{3}$$

Compared with the traditional drive system, the small volume of the film capacitor cannot maintain the dc-link voltage constant. The dc-link voltage will fluctuate with twice the frequency of grid voltage and it can be expressed as

$$\begin{aligned} u_{\rm dc} &= |U_g \sin(\omega_g t + \varphi_g)| \\ &= U_g \sin(\omega_g t + \varphi_g) \cdot \mathrm{sgn}(\sin(\omega_g t + \varphi_g)). \end{aligned} \tag{4}$$

As a result, $P_{\rm dc}$ can be calculated as follows:

$$\begin{aligned} P_{\rm dc} &= u_{\rm dc} C_{\rm dc} \frac{du_{\rm dc}}{dt} \\ &= u_{\rm dc} C_{\rm dc} \frac{d}{dt} \{U_g \sin(\omega_g t + \varphi_g) \cdot \mathrm{sgn}(\sin(\omega_g t + \varphi_g))\} \\ &= \frac{1}{2} U_g^2 C_{\rm dc} \omega_g \sin(2(\omega_g t + \varphi_g)) \end{aligned} \tag{5}$$

where $C_{\rm dc}$ is the capacitance of the film capacitor and sgn() is the sign function.

Ignoring the switching loss of the inverter, the motor power can be regarded as the inverter power $P_{\rm inv}$. Therefore, the inverter power $P_{\rm inv}$ can be calculated as

$$P_{\rm inv} = 1.5\left(\vec{u}_{\rm dq} \cdot \vec{i}_{\rm dq}\right) = 1.5(u_d i_d + u_q i_q) \tag{6}$$

$$u_d = R_s i_d + L_d \frac{di_d}{dt} - \omega_r L_q i_q \tag{7}$$

$$u_q = R_s i_q + L_q \frac{di_q}{dt} + \omega_r L_d i_d + \omega_r \psi_f \tag{8}$$

where u_d, u_q, i_d, i_q, R_s, L_d, L_q, ψ_f, and ω_r are the voltages and currents of the motor in *d*–*q* rotating reference frame, the stator resistance, the *d*- and *q*-axis inductances, the flux of the permanent magnet, and the rotor angular speed, respectively.

Based on the power analysis of the drive system, the solution to achieve high power factor and low THD of the grid current is to ensure the grid input power to be sinusoidal. As shown in (3), the grid input power depends on the film capacitor power and the inverter power. The film capacitor power can be calculated by the fluctuated dc-link voltage according to (5), which cannot be controlled directly. Meanwhile, the sum of the film capacitor power per cycle is zero, and the magnitude of the power is much smaller than the inverter power. As a result, the approach to control the grid input power is to regulate the inverter power effectively.

III. Proposed Inverter Power Control Method

Fig. 3 shows the block diagram of the proposed inverter power control strategy. The power PR controller is applied to control the inverter power, which mainly generates the *q*-axis current reference. However, the inverter power loop cannot effectively control the inverter power, and the detailed analysis will be presented in Section III-B. As a result, a power compensation method based on the dc-link voltage regulation is adopted to diminish the power control error. Meanwhile, the output voltage modification block aims to impose the output of the dc-link voltage regulation to the decoupled voltage vectors. The generation of the current reference for flux weakening should take the dc-link voltage fluctuation into consideration. Additionally, as the over-modulation of space vector pulse width modulation (SVPWM) distorts the applied voltage to the motor, the stator current will contain many ripples, which will lead to the distortions of the grid current. In order to reduce the harmonics of the grid current, the proposed SVPWM modulation method ensures that the magnitude of the voltage vector satisfies the maximum output voltage circle of the inverter. The detailed analysis of the proposed control method is illustrated as follows.

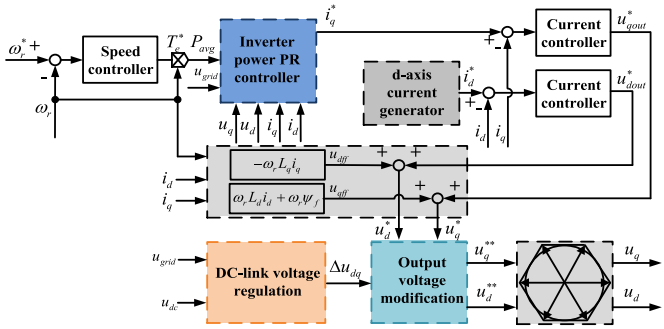

Fig. 3. Overall diagram of the proposed inverter power control strategy.

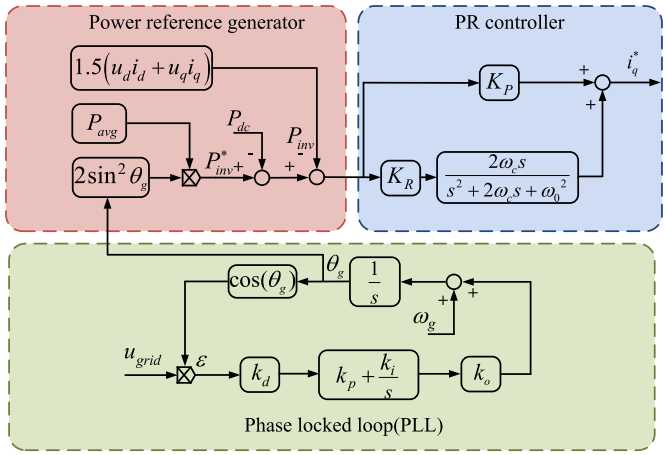

Fig. 4. Block diagram of the inverter power controller.

A. Inverter Power Control Loop

Fig. 4 shows the block diagram of the inverter power controller. As shown in (3), the grid input power consists of the film capacitor power and the inverter power. According to (5), the average power of the film capacitor is zero and the average grid input power is equal to the average inverter power. The average inverter power reference $P_{\rm avg}$ is regulated by the product of the torque reference T_e^* and the angular speed ω_r. The grid voltage

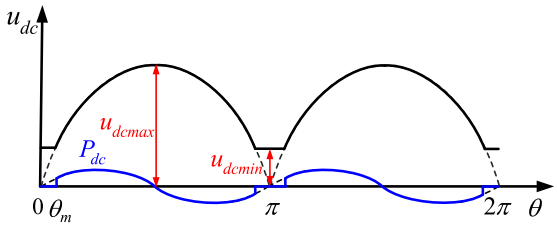

Fig. 5. Typical waveform of the dc-link voltage.

phase θ_g is detected by a phase-locked loop. Then P_{avg} is regulated by a sinusoidal waveform to generate the grid input power reference P^*_{inv}, which fluctuates with twice the frequency of the grid voltage.

Actually, the dc-link voltage cannot decrease to zero when the load is not large enough, and the typical waveform of the dc-link voltage is shown in Fig. 5. The film capacitor power P_{dc} is related to the dc-link voltage and can be calculated as follows:

$$P_{\text{dc}} = \begin{cases} 0 & \theta \in [0\ ,\ \theta_m\ ) \cup (\pi - \theta_m\ \ ,\ \pi] \\ \dfrac{1}{2} U_g^2 C_{\text{dc}} \omega_g \sin\ (2\theta_g) & \theta \in [\theta_m\ ,\pi - \theta_m] \end{cases} \tag{9}$$

where θ_g and θ_m denote the phase of the grid voltage and the initial conduction phase of the grid current, respectively.

The inverter power control loop is established by regarding the calculation of the motor output power as the power feedback P_{inv}, which also represents the mechanical load of the motor. It can be seen that the power signals in the inverter power control loop are the periodic sinusoidal signals. Hence both the repetitive controller and PR controller can achieve better performance than the PI controller, which is effective to the dc signals. The repetitive controller and PR controller are based on the internal model theory, which can realize high precision control for the feedback system by specific controllers combined with the internal model of input signal or disturbance signal. The repetitive controllers are applied successfully to track the periodic input signal or reject the periodic disturbance. As for the sinusoidal signals, the PR controller containing the corresponding internal model is applied to optimize the control performance.

The repetitive controller needs several periods to learn the signal model and eliminate the errors by the sum of errors in the previous periods. As for the PR controller, the signal model has been previously set based on the internal model of the sinusoidal signal. Therefore, as for the sinusoidal signals, the control performance of PR controller can be better than that of the repetitive controller. Meanwhile, the repetitive controller should be combined with a PI controller to satisfy the basic system requirements on closed-up bandwidth, loop gain, etc. More parameters need to be designed than that of PR controller. As a result, the parameter determination and system stability consideration applying repetitive controller will be trivial compared with the PR controller. Hence, the PR controller is applied in the proposed inverter power control loop to achieve better performance and a simple control block, which is easy to determine the parameters.

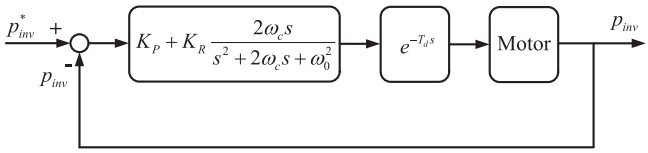

Fig. 6. Power control loop of the PR controller.

The PR controller can be expressed as follows:

$$G_{\text{PR}}(s) = K_P + K_R \frac{2\omega_c s}{s^2 + 2\omega_c s + {\omega_0}^2} \tag{10}$$

where K_P and K_R are the proportional gain and the resonant gain, ω_0 is the resonant frequency and ω_c is the cutoff frequency. The output of PR controller depends on the error between inverter power reference and actual inverter power, which can be regarded as the q-axis current reference. As for the steady state, the average q-axis current is proportional to the load torque and the instantaneous value will fluctuate with twice the frequency of the grid voltage. Therefore, the output of PR controller contains the twice frequency component and the high-frequency component for the stator current regulation. The values of K_P and K_R can be determined as follows [32]–[34].

The power control loop of PR controller can be shown in Fig. 6, where T_d is the time delay of the control loop and the motor can be simplified as a *RL* circuit. The open loop transfer function can be given by

$$G\,(s) = K_P \left(1 + \frac{2\omega_c s}{T_P\ (s^2 + 2\omega_c s + \omega_0^2)}\right) \cdot e^{-T_d s} \cdot \frac{1}{R\,(1 + sT_i)} \tag{11}$$

where $T_P\ =\ K_P/K_R$ and $T_i\ =\ L/R$.

The phase angle of the open loop transfer function $G(s)$ at the cross over frequency ω_f is given by

$$\begin{aligned} \angle G(j\omega_f) &= \angle \left\{ \frac{K_P}{R} \left(1 + \frac{2j\omega_f\omega_c}{T_P \left\{ \left(\omega_0^2 - \omega_f^2\right) + 2j\omega_f\omega_c \right\}} \right) \right. \\ &\quad \left. \times \frac{e^{-j\omega_f T_d}}{1 + j\omega_f T_i} \right\} \\ &= (-\pi + \varphi_m) \\ &\approx \tan^{-1}\left(\omega_f T_P/2\omega_c\right) - \pi/2 - \omega_f T_d \\ &\quad - \tan^{-1}\left(\omega_f T_i\right) \end{aligned} \tag{12}$$

where φ_m represents the required stability phase margin, which is usually taken as 40° in theory. The phase margin can be represented as

$$\varphi_m \approx \tan^{-1}\left(\omega_f T_P/2\omega_c\right) - \omega_f T_d. \tag{13}$$

The maximum value of ω_f for a given φ_m can be represented as

$$\omega_{f(\max)} = \frac{\pi/2 - \varphi_m}{T_d}. \tag{14}$$

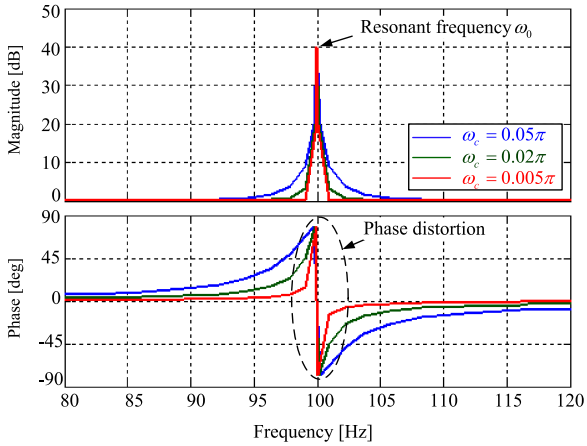

Fig. 7. Bode diagram of PR controller of different ω_c values.

The maximum magnitude of K_P can be achieved by setting the open loop gain at this frequency $\omega_{f(\max)}$ to unity, which gives

$$K_P = R\omega_{f(\max)}T_P \frac{\sqrt{1+\left(\omega_{f(\max)}T_i\right)^2}}{\sqrt{\left(\omega_{f(\max)}T_P\right)^2+\left(2\omega_c\right)^2}}. \tag{15}$$

Therefore, the magnitude of K_P can be represented as

$$K_P = \omega_{f(\max)}L. \tag{16}$$

The magnitude of K_R can be maximized by making

$$\tan^{-1}\left(\omega_{f(\max)}T_P/2\omega_c\right) \approx \pi/2 \tag{17}$$

which gives

$$T_p = \frac{20\omega_c}{\omega_{f(\max)}}. \tag{18}$$

The values of K_P and K_R are determined by the presented method when the equivalent *RL* circuit of the power control loop is regarded as the *q*-axis *RL* circuit. In this drive system, the coupled inverter power between *d*- and *q*-axis leads the *d*-axis inductance to affect the accuracy of the equivalent *RL* circuit. The parameters of PR controller need to be tuned in practical application to optimize the control performance. Fortunately, the tuning is relatively simple since the values of the *d*- and *q*-axis inductance are in the same order of magnitude.

As the frequency of the grid voltage is 50 Hz and the dc-link voltage rectified by the single-phase diode rectifier fluctuates with 100 Hz, the resonant frequency ω_0 should be set as 100 Hz. Meanwhile, the PR controller can achieve better performance when the cutoff frequency ω_c is set lower to obtain a higher gain for the inverter power reference signal. However, it should be noted that the lower value of ω_c may result in the instability of the drive system for the sharper phase distortion. The Bode diagram of the PR controller is shown in Fig. 7.

B. Inverter Power Compensation

1) Analysis of the Control Performance Only Adopting the Inverter Power Control Loop: The inverter power controller is introduced in Section III-A. While the error between the power reference P^*_{inv} and the actual feedback power P_{inv} is difficult to be eliminated only by adopting the PR controller in the inverter power control loop. The PR controller can obtain better performance for the fluctuated inverter power component. However, as for the fluctuated current signals, the traditional PI current controllers will limit the control performance. Meanwhile, the inverter power is coupled between *d*- and *q*-axes, and it can be presented as follows:

$$P_{\text{inv}} = 1.5\left[i_d^2R_s + i_dL_d\frac{di_d}{dt} + i_di_q\omega_r\left(L_d - L_q\right) + i_q^2R_s + i_q\left(L_q\frac{di_q}{dt} + \omega_r\psi_f\right)\right]. \tag{19}$$

As the feedback of the inverter power only has an effect on i_q reference and the regulation of i_d does not depend on the inverter power control loop, the reference of i_q generated from the PR controller is not the optimal matching. Once taking the relationship of the coupled inverter power in the *d*–*q* reference frame into consideration, the accurate regulation of i_d is not easy to realize. As a result, it is also difficult to separate the coupled power between *d*- and *q*-axis completely.

Therefore, it is necessary to adopt an additional inverter power compensation block to reduce the inverter power control error, which can realize the actual power feedback tracking the power reference better. Meanwhile, the bandwidth of current PI controllers can be set lower, which benefits the stability of the drive system.

2) Proposed Inverter Power Compensation Method Based on the DC-Link Voltage Regulation: A novel power compensation method based on the dc-link voltage regulation is illustrated in this part. The traditional drive system needs a PFC circuit to ensure that the grid current can satisfy the standard requirements of EN-61000-3-2. The PFC circuit also blocks the grid input side and the inverter output side. Due to the elimination of the PFC circuit in the electrolytic capacitor-less drive system, the grid input side and inverter output side have been connected by the dc-link directly. The distorted grid input current caused by the distorted inverter output power is reflected by the dc-link voltage. Hence, the distorted inverter power can be detected by the dc-link voltage and the additional power compensation can be realized by the dc-link voltage regulation.

The direct inverter power control method in [31] calculated the power control error between inverter power reference and actual inverter power for the direct inverter power control. The advantages of this method are the accurate inverter power regulation and good grid current performance, which is strictly based on the power relationships of the drive system. The inverter power reference of the method in [31] was generated by the product of actual motor speed and the output of speed controller. As the motor speed fluctuates with the severely fluctuated dc-link voltage, the output of speed controller cannot remain a constant value. Hence, the bandwidth of speed controller should be set lower to overcome the fluctuated feedback speed and generate an average power reference value, which will influence the dynamic performance of the speed control.

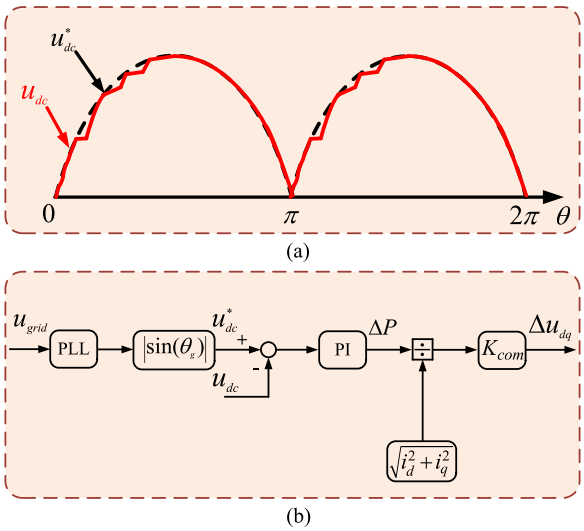

Fig. 8. Scheme of the inverter power compensation. (a) DC-link voltage reference and the actual distorted dc-link voltage. (b) Block diagram of the dc-link voltage regulation.

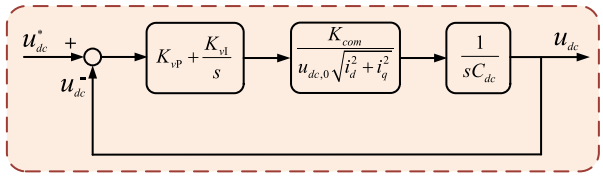

Fig. 9. Small signal block diagram of the dc-link voltage control.

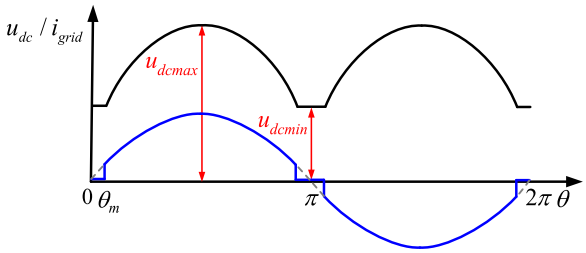

Fig. 10. Grid current corresponding to the fluctuated dc-link voltage.

Meanwhile, the implementation of the current reference generation and the over-modulation method with maintenance of output power is more difficult due to the increased computation. As for the proposed method, there is no requirement on the speed controller and it is easy to realize due to the simple structure and the reduced calculation.

According to the circuit topology of Fig. 1, the inverter power can be calculated as

$$P_{\text{inv}} = u_{\text{dc}} i_{\text{inv}} = u_{\text{dc}} \left(i_{\text{grid}} - C_{\text{dc}} \frac{du_{\text{dc}}}{dt} \right) \tag{20}$$

where i_{inv} represents the dc-link current of the inverter.

Generally, the dc-link voltage can be calculated as shown in (4). However, if the inverter power cannot be controlled effectively, the irregular inverter power will distort the dc-link voltage. The Fourier of the actual dc-link voltage can be expressed as

$$u_{\text{dc}} = u_{\text{dc},0} + \sum_{k=1}^{n} u_{\text{dc},k} \sin\left(2k\omega_g t + \varphi_{\text{dc}}\right) \tag{21}$$

where $u_{\text{dc},0}$, $u_{\text{dc},k}$, and φ_{dc} are the offset value, the amplitudes, and the phases of kth harmonic components of dc-link voltage, respectively.

Therefore, the inverter power control error can be detected by the distortion of the dc-link voltage as shown in Fig. 8(a). The proposed power compensation method based on the dc-link voltage regulation is applied to improve the inverter power control performance, which is shown in Fig. 8(b). The dc-link voltage reference is generated by the sine operation of the estimated phase of the grid voltage. A PI controller is applied to regulate the dc-link voltage. The output of the PI controller represents the power error ΔP that can be calculated as follows:

$$\Delta P = \left(K_{vP} + \frac{K_{vI}}{s} \right) \left(u_{\text{dc}}^* - u_{\text{dc}} \right) \tag{22}$$

where K_{vP} and K_{vI} represent the proportional gain and the integral gain of the dc-link controller, u_{dc}^* and u_{dc} represent the dc-link voltage reference and the actual dc-link voltage, respectively.

Then, ΔP is divided by the magnitude of the current vector, which represents the magnitude of the modified voltage Δu_{dq} in the d–q reference frame. Actually, the modified voltage Δu_{dq} will lead to the additional motor power ΔP, which can affect Δi_{inv}. The relationship can be given by

$$\Delta i_{\text{inv}} = \frac{\Delta P}{u_{\text{dc},0}}. \tag{23}$$

An inductance filter is applied to improve the quality of the grid current in the electrolytic capacitor-less drive system, which can stabilize the grid current and reduce the impact caused by Δi_{inv}. As a result, the current of the dc-link film capacitor Δi_{dc} is regulated by Δi_{inv}, which can shape the dc-link voltage Δu_{dc} as

$$\Delta u_{\text{dc}} = \frac{1}{C_{\text{dc}}} \int \Delta i_{\text{dc}}\left(t\right) dt. \tag{24}$$

Therefore, the small signal block diagram of the dc-link voltage regulation can be simply expressed as Fig. 9. As for the value of K_{com}, it will be discussed in Section III-C. The establishment of the dc-link control loop can explain the relationship between the motor power and the dc-link voltage, which can shape the dc-link voltage effectively. Meanwhile, the control loop can be regarded as a first-order system, and it is easy to design the parameters of PI controller. Therefore, the dc-link voltage regulation can effectively eliminate the distorted inverter power and improve the power control performance.

3) Generation of DC-Link Voltage Reference for the Proposed DC-Link Voltage Regulation: It can be seen from Fig. 10 that u_{dcmin} is closely related to the conduction angle of the diode rectifier, which has an important effect on the grid current harmonics. The grid current shown in Fig. 10 can be approximately

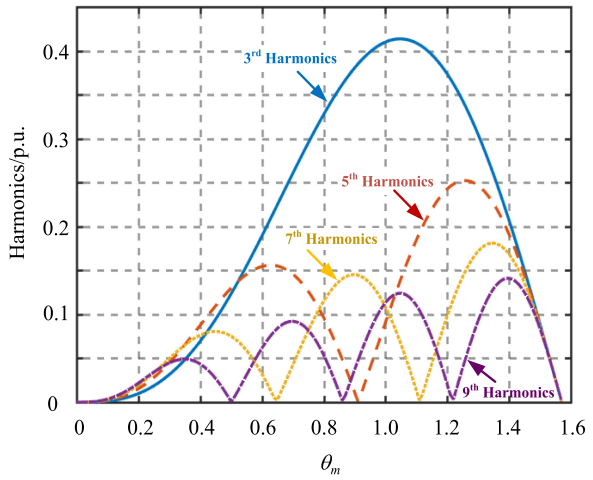

Fig. 11. Harmonics of grid current with respect to the initial conduction phase θ_m.

represented as

$$i_{\text{grid}} = \begin{cases} I_g \sin\theta, & \theta \in [\theta_m, \pi - \theta_m] \cup [\pi + \theta_m, 2\pi - \theta_m] \\ 0, & \theta \in [0, \theta_m] \cup [\pi - \theta_m, \pi + \theta_m] \cup [2\pi - \theta_m, 2\pi] \end{cases}. \tag{25}$$

As the function of i_{grid} can be regarded as an odd one, the Fourier analysis of i_{grid} is the sinusoidal series, which can be calculated as

$$i_{\text{grid}} = \sum_{n=1}^{\infty} b_n \sin(nx)$$

$$b_n = \frac{2}{\pi} \int_{\theta_m}^{\pi - \theta_m} I_g \sin\theta \sin(n\theta)\, d\theta, n = 1, 3, 5, 7, \ldots \tag{26}$$

The Fourier coefficients b_n can be represented as

$$b_n = \frac{I_g}{\pi} \left(\frac{1}{n+1} \sin((n+1)\theta_m) - \frac{1}{n-1} \sin((n-1)\theta_m) \right). \tag{27}$$

It can be seen that b_n is related to I_g. For example, if the value of I_g is unit, the grid current harmonics with respect to θ_m can be shown in Fig. 11.

The other orders of the grid current harmonics can be calculated by (27). As a result, the value of θ_m can be obtained to satisfy the harmonic standards, which are shown in Table I. Hence u_{dcmin} can be determined according to the value of grid currents, which can make the system satisfy the harmonic standards. The detailed values under different amplitude of grid currents can be shown in Fig. 12, and it can be seen that the dc-link voltage reference u_{dcmin} decreases as the grid current increases.

C. Output Voltage Modification

The outputs of the current controllers are decoupled by the feed-forward voltage u_{dff} and u_{qff} to generate the voltage

TABLE I
HARMONIC STANDARDS OF EN61000-3-2

Harmonics[nth]	Standards[A]
2	1.08
3	2.30
4	0.43
5	1.14
6	0.3
7	0.77
8	0.23
9	0.40
10	0.18
11	0.33
12	0.15
13	0.21
Even harmonics($14 \le n \le 40$)	1.84/n
Odd harmonics($15 \le n \le 39$)	2.25/n

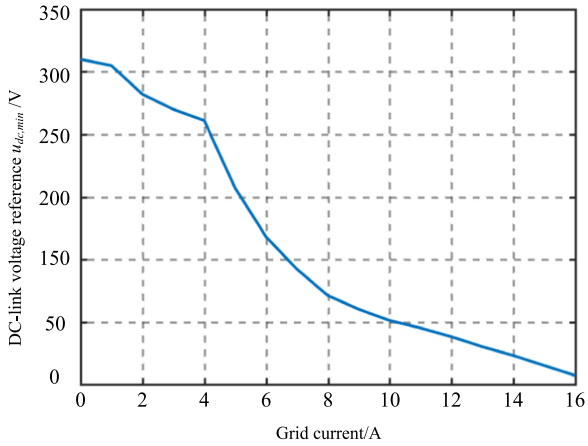

Fig. 12. Determination of dc-link voltage reference with respect to the altitude of grid current.

vector reference u_{dq}^*. Whereas the output of the dc-link voltage regulation shown in Fig. 8 needs to be imposed to the final voltage vector reference. The purpose of the output signal Δu_{dq} is to modify the inverter power, which also can be regarded as a voltage disturbance for the closed-loop control system. Therefore, the smaller the magnitude of the imposed voltage vector is, the less the effect of the voltage disturbance will be on the drive system. The additional effect of the voltage vector on the motor current has been considered in the voltage modification module in [31]. Hence, the optimized voltage modification vectors are the ones with the shortest distance between the final voltage vector and the feedforward voltage vector. In the proposed output voltage modification method, the feed-forward voltage vector and the output of current controller are treated as a whole voltage vector u_{dq}^*, which owns the smallest magnitude for certain power modification because the effect of the additional voltage vector on the motor current is not obvious. Hence, the compromise between the consideration of the effect on the motor current in [31] and the reduced calculation of the proposed method is tolerable. The imposed voltage vector in the d–q reference frame is shown in Fig. 13(a), and the possible direction of voltage vector is infinite, which means the

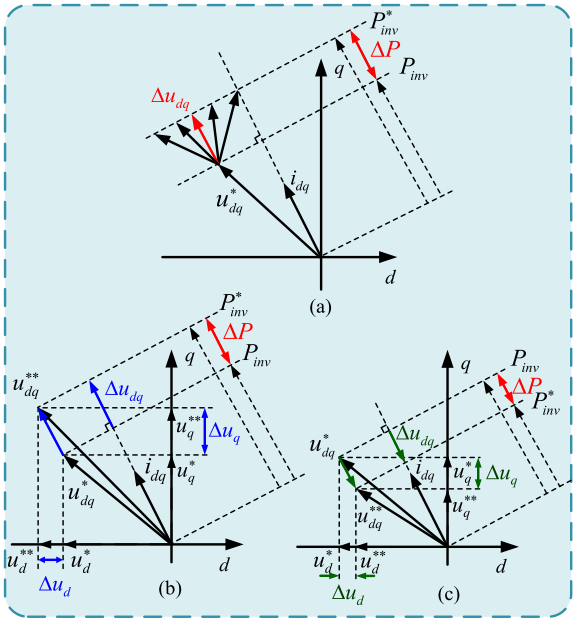

Fig. 13. Scheme of the output voltage modification. (a) Selection of the modified voltage direction. (b) $P_{\rm inv} < P^*_{\rm inv}$. (c) $P_{\rm inv} > P^*_{\rm inv}$.

value of $K_{\rm com}$ is various. However, the direction paralleled to the current vector is the optimization, because the magnitude of the voltage is the smallest one to the same inverter power modification. Meanwhile, $K_{\rm com}$ can be regarded as a unity gain. Fig. 13(b) shows the scheme of the synthetic voltage vector modification when the inverter power error $\Delta P > 0$. It means that $P_{\rm inv}$ is smaller than $P^*_{\rm inv}$. In the figure, Δu_d and Δu_q are the d- and q-axis modification voltages, respectively. By applying the voltage modification block, the final voltage reference $u^{**}_{\rm dq}$ can decrease the inverter power error effectively. Fig. 13(c) shows the situation that $\Delta P < 0$ and the direction of $\Delta u_{\rm dq}$ is opposite to the one in Fig. 13(b) in order to decrease the inverter power. As a result, the performance of inverter power control can be improved by applying the modified voltage.

D. Effects of the Fluctuated DC-Link Voltage on Inverter Output Voltage and Maximum Motor Speed

The motor speed limitation is related to the source voltage, dc-link voltage, and loads. The drive system should meet the voltage and current constraint to guarantee the normal motor operation. As for the electrolytic capacitor-less drive system, the maximum operating speed will be determined by the fluctuated dc-link voltage for the remarkably reduced dc-link capacitance compared with the traditional drive system. The dc-link voltage is fluctuated with the grid voltage as shown in Fig. 5. The inner diameter of the voltage hexagon is synchronous with the fluctuated dc-link voltage, which will limit the average inverter output voltage and the maximum operating speed.

The attenuation coefficient λ of the average inverter output voltage can be represented as follows:

$$\lambda = \frac{\int_{\theta_m}^{\pi-\theta_m} u_{\rm dc\,max}\sin\theta d\theta + 2u_{\rm dcmin}\theta_m}{u_{\rm dc\,max}\pi} \tag{28}$$

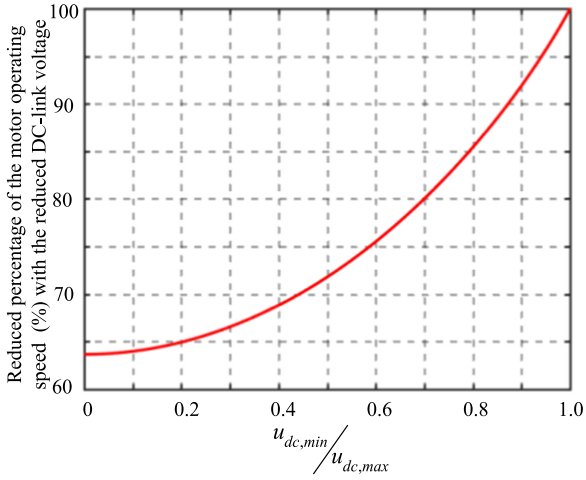

Fig. 14. Relationship between the dc-link voltage and the reduced percentage of the motor operating speed.

where the initial conduction phase θ_m can be calculated as follows:

$$\theta_m = \arcsin\left(\frac{u_{\rm dcmin}}{u_{\rm dcmax}}\right), \theta_m \in [0, \pi/2]. \tag{29}$$

It can be easily proved that the grid voltages with different frequencies almost provide the same average inverter output voltage because of the characteristic of the sine function. Generally, because of the voltage and current rating of the inverter and the motor itself, the maximum operation speed of the machine is limited by the voltage and current constraint. The voltage and current constraint can be represented as

$$u_d^2 + u_q^2 = \left(R_s i_d + L_d\frac{di_d}{dt} - \omega_r L_q i_q\right)^2 + \left(R_s i_q + L_q\frac{di_q}{dt} + \omega_r L_d i_d + \omega_r\psi_f\right)^2 \le \frac{u_{\rm dc}^2}{3},$$
$$i_d^2 + i_q^2 \le i_s^2 \tag{30}$$

where i_s represents the maximum current and it can be simplified as

$$(L_q i_q)^2 + (L_d i_d + \psi_f)^2 \le \frac{u_{\rm dc}^2}{3\omega_r^2}, \quad i_d^2 + i_q^2 \le i_s^2 \tag{31}$$

for the condition ignoring the voltage drop caused by the stator resistance and assuming the steady-state operation. As for the drive system, the voltage constraint can be represented as

$$(L_q i_q)^2 + (L_d i_d + \psi_f)^2 \le \frac{u_{\rm dc,max}^2}{3}\left(\frac{\lambda}{\omega_r}\right)^2. \tag{32}$$

It can be seen that the maximum operating speed is proportional to the attenuation coefficient λ and the reduced percentage of the operating speed is consistent with λ. The reduced percentage of the speed can be shown in Fig. 14. It can be concluded that the operating speed reduces with the decrease of $u_{\rm dcmin}/u_{\rm dcmax}$ and the minimum percentage is 63.7% when the dc-link voltage decreases to zero.

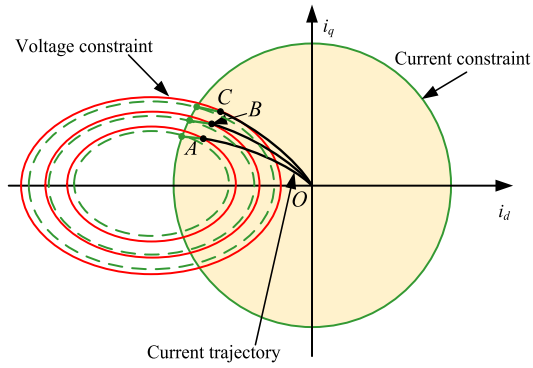

Fig. 15. Voltage current constraint of motor operation with different loads.

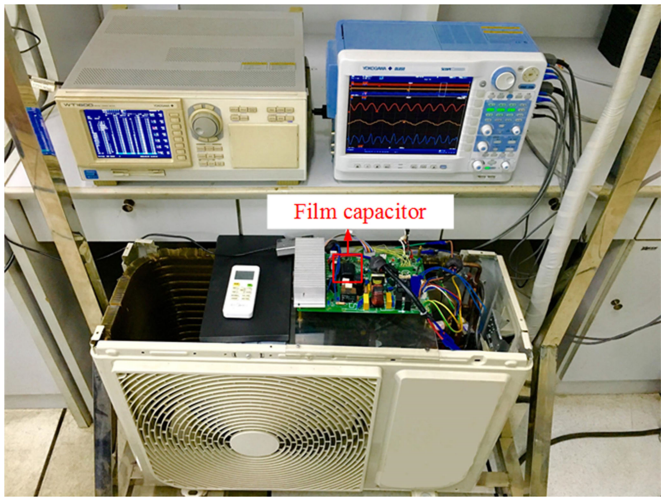

Fig. 16. Experimental platform (air-conditioner).

The constraints and current trajectory with different loads are shown in Fig. 15. The solid curves represent the determined voltage constraint and the dotted curves represent the voltage constraint corresponded to the current constraint. The intersection points of the determined voltage constraint and current trajectory represent actual motor operating points. The magnitude of d- and q-axis current will increase to supply the motor torque for the loads as the d-axis current increases. It can be seen that the intersection of the voltage constraint and the current constraint is the motor operating region. As for the electrolytic capacitor-less drive system, the voltage constraint will determine the maximum operating speed because of the remarkably reduced dc-link capacitance. The operating points can be obtained by the combination of the determined voltage constraint and the current trajectory with different loads as shown in Fig. 15.

IV. Experimental Results

For the purpose of demonstrating the effectiveness of the proposed inverter control method, experiments are performed on an air conditioner drive platform without electrolytic capacitors in the dc-link. Fig. 16 shows the experimental platform,

TABLE II
Parameters of the Experimental Platform

Parameters	Value
Grid voltage	220 Vrms
Grid frequency	50 Hz
Film capacitor	20 μF
Line filter inductor	5 mH
Switching frequency	10 kHz
Sampling frequency	10kHz
Rated power	1.0 kW
Rated speed	3000 r/min
Stator resistor	1.48 Ω
d-axis inductance	7.9 mH
q-axis inductance	11.7 mH
Flux linkage of rotor	0.11 Wb
Number of pole pairs	3

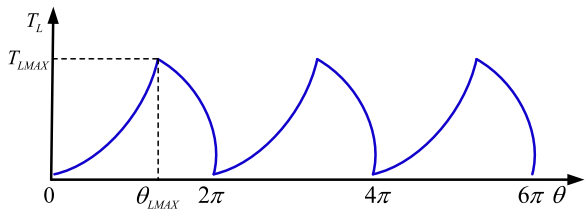

Fig. 17. Load torque of the single rotary compressor.

and the parameters of platform are shown in Table II. The whole control algorithm is realized with a digital signal processor TMS320F28034. As the mechanical sensors cannot be installed on the compressor, the motor is operated by the sensorless control. The bandwidth of current PI controllers is selected as 200 Hz to ensure the stability of the system, the proportional gain K_P, the resonant gain K_R and the cutoff frequency ω_c of the PR controller are 1.0, 0.1, and 0.02 π, respectively. The power meter WT1600 is used to measure the harmonics of the grid current. The mechanical load characteristic of the single rotary IPMSM compressor air conditioner is shown in Fig. 17, and it can be seen that the load torque has a large variation per mechanical cycle, which is determined by the operational principle of the single rotary compressor.

Fig. 18 shows the experimental results with and without applying the proposed inverter power control loop adopting PR controller and the dc-link voltage regulation strategy when the compressor operates at 3000 r/min. The left waveforms from top to bottom show the dc-link voltage, the actual inverter power, the grid current, and the motor current, respectively. Meanwhile, the Fourier analysis of the dc-link voltage and grid current are shown in the right part. In Fig. 18(a), without the inverter power control loop and the dc-link voltage regulation strategy, it can be seen that the inverter power is not under control and the resonance between the inductor of input filter and the dc-link film capacitor is obvious that cannot be effectively suppressed. The resonance frequency of the drive system is approximately 500 Hz when the line inductor is 5 mH and the film capacitor is 20 μF. It can be seen that the dc-link voltage fluctuates severely and the harmonics of grid current far exceed the standards of

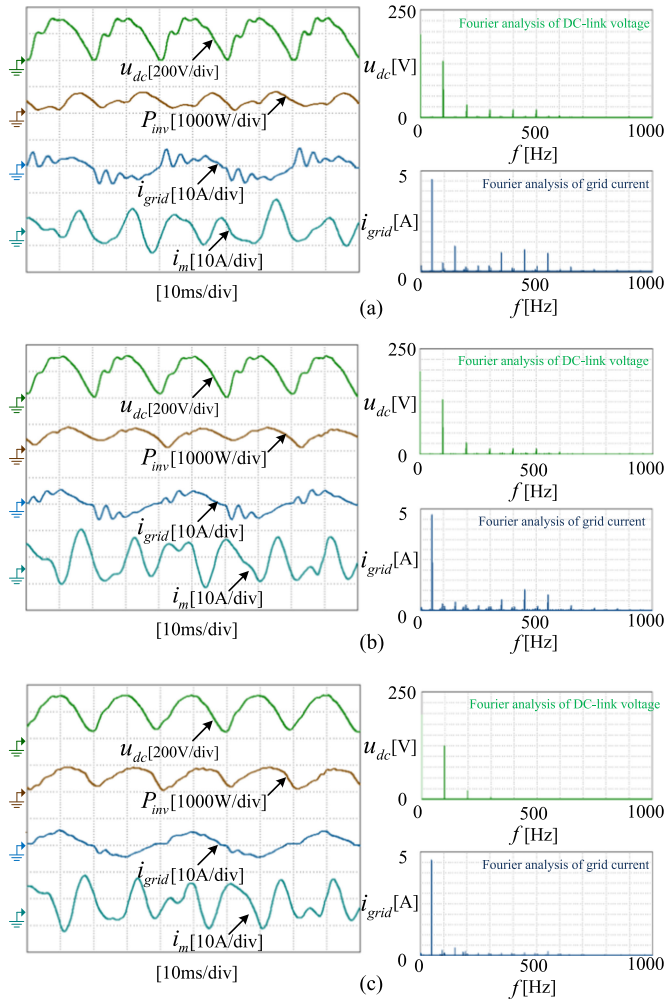

Fig. 18. Experimental waveforms when the compressor operates at 3000 r/min. (a) Without the inverter power control loop (power factor = 0.891, THD = 51.3%). (b) Only using the inverter power control loop with PR controller (power factor = 0.912, THD = 37.8%). (c) Combining the proposed dc-link voltage regulation strategy with the inverter power control loop adopting PR controller (power factor = 0.981, THD = 16.0%).

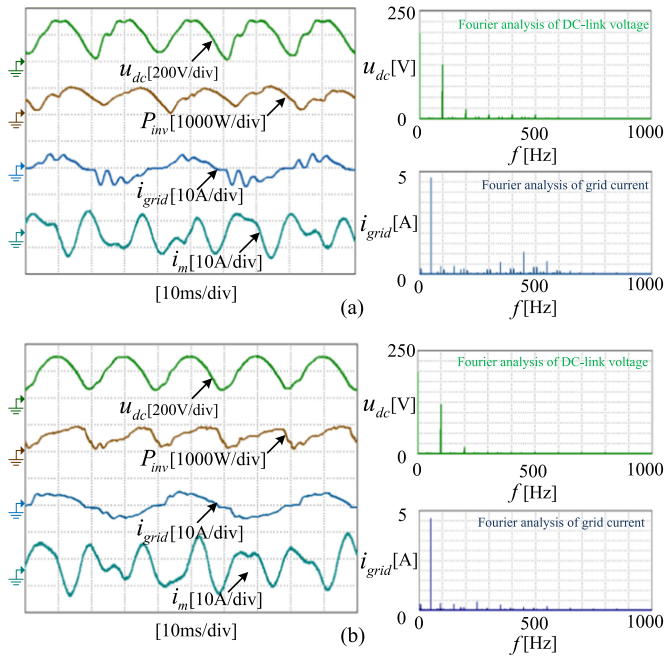

Fig. 19. Experimental waveforms adopting repetitive controller when the compressor operates at 3000 r/min. (a) Only using the inverter power control loop with repetitive controller (power factor = 0.903, THD = 38.9%). (b) Combining the proposed dc-link voltage regulation strategy with the inverter power control loop adopting repetitive controller (power factor = 0.973, THD = 17.5%).

EN61000-3-2, and the harmonics around the resonant frequency are obviously serious. At the same time, the compressor is unable to operate at high speed because the irregular inverter power and the severe resonance will lead the drive system unstable. In Fig. 18(b), the inverter power control loop with PR controller is applied and the power factor and THD of the grid side are 0.912 and 37.8%. It can be seen that the grid side performance is improved compared with that in Fig. 18(a). Combined with the proposed dc-link voltage regulation strategy, the inverter power control loop with PR controller is applied in Fig. 18(c). It can be seen that the grid side performance is obviously improved and also the harmonics of grid current can be obviously suppressed. The power factor and THD of the grid side are 0.981% and 16.0%. It can be concluded from Fig. 18 that only using the inverter power control loop is difficult to effectively control the inverter power and suppress the harmonics of the grid current. The fluctuation of the dc-link voltage is not under control, which reduces the conduction angle of the diode rectifier and limits the improvement of the power factor. The resonance can be suppressed while the performance is limited. Based on the inverter power control loop, better performance can be achieved by applying the proposed dc-link voltage regulation, which can also shape the dc-link voltage effectively despite the large load variation of the compressor. Meanwhile, the resonance can be effectively suppressed for the enhanced inverter power control performance. As a result, it can be seen from the Fourier analysis that the harmonics of dc-link voltage and grid current can be obviously suppressed.

In order to compare the control performance of PR controller and repetitive controller, in Fig. 19(a), the repetitive controller is applied in the inverter power control loop and the power factor and THD of the grid side are 0.903% and 38.9%.The corresponding power factor and THD of the PR controller are 0.912% and 37.8%. Combined with the proposed dc-link voltage regulation strategy, the inverter power control loop with repetitive controller is applied in Fig. 19(b). The power factor and THD of the grid side are 0.973% and 17.5% and the corresponding power factor and THD of the PR controller are 0.981% and 16.0%. It can be seen that the control performance of PR controller is better than the applied repetitive controller because the PR controller is more effective to the sinusoidal signals than the repetitive controller as described in the Section III.

Fig. 20 shows the experimental results applying the inverter power control loop with PR controller and the proposed dc-link voltage regulation strategy when the compressor operates at 5000 r/min. It can be seen that the control performance becomes better as the compressor speed increases. The motor

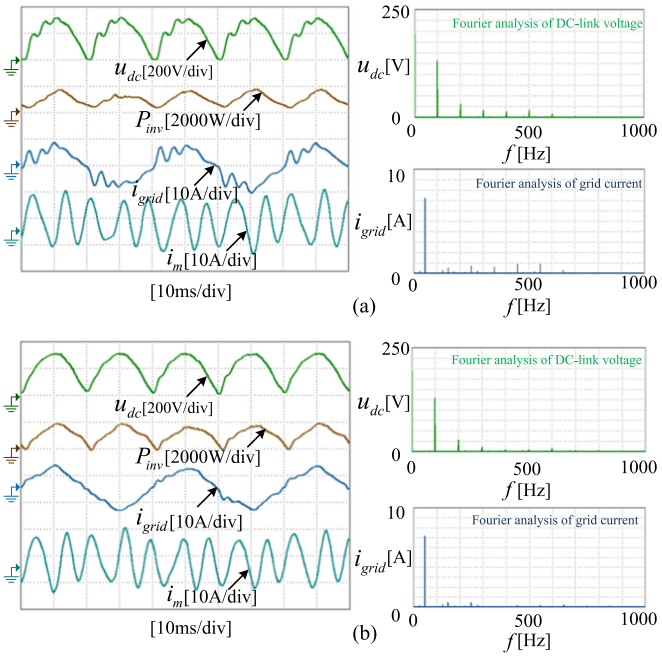

Fig. 20. Experimental waveforms when the compressor operates at 5000 r/min. (a) Only using the inverter power control loop with PR controller (power factor = 0.964, THD = 26.3%). (b) Combining the proposed dc-link voltage regulation strategy with the inverter power control loop adopting PR controller (power factor = 0.991, THD = 10.7%).

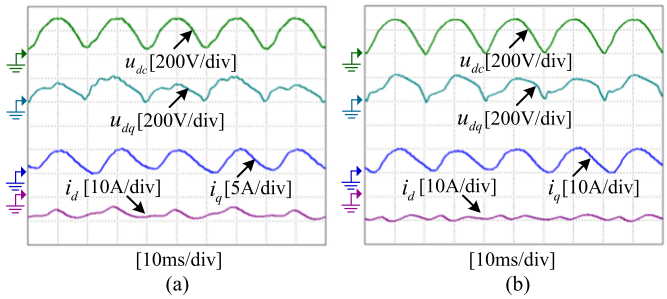

Fig. 21. Experimental waveforms of the magnitude of voltage vector, d- and q-axis current components using the proposed inverter power control method. (a) 3000 r/min. (b) 5000 r/min.

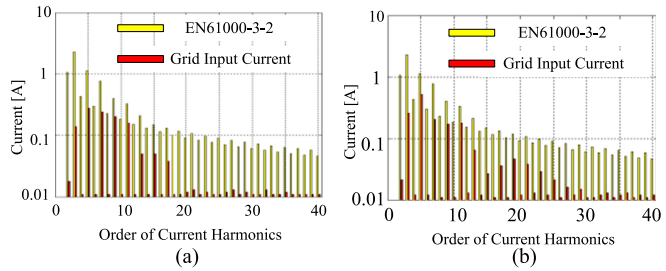

Fig. 22. Comparison with the EN61000-3-2 limits and the grid current harmonics applying the proposed inverter power control method. (a) 3000 r/min. (b) 5000 r/min.

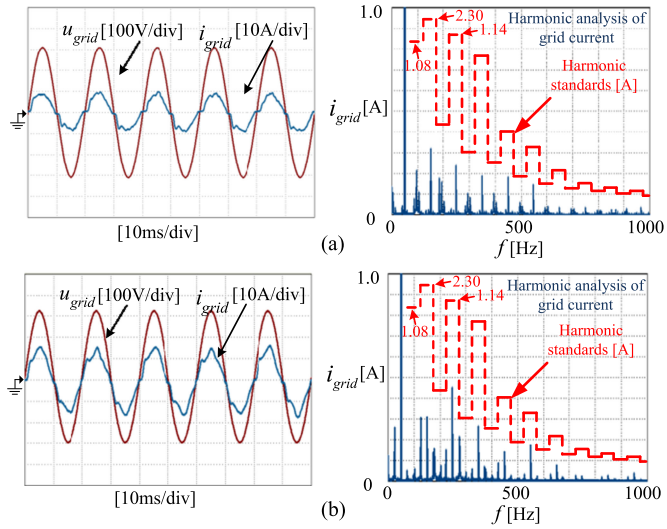

Fig. 23. Experimental waveforms of the grid voltage and grid current and the harmonic analysis of grid current. (a) 3000 r/min. (b) 5000 r/min.

current becomes more regular than that of the motor operates at 3000 r/min, which means that the effect of the load torque fluctuation on the drive system is reduced and it can benefit the control performance.

In order to compare the efficiency, the grid input power is measured by a power meter WT1600, which is calculated by the root mean square values of the grid voltage and current. The measured values are 569, 571, and 573 W by applying the conventional methods [in Fig. 18(a)] and the proposed method [in Fig. 18(b) and (c)], respectively. It can be seen that the efficiency of the proposed method is slightly lower because of the fluctuated motor power, which can motivate high-order power ripple. As a result, the power ripple will increase the harmonic iron loss compared with the drive system that outputs constant motor power. Meanwhile, the high-order power ripple will increase the eddy current loss, which can also reduce the motor drive efficiency. It can be concluded that the desired fluctuated inverter power can benefit the grid side quality, whereas the caused power ripple will slightly reduce the drive system efficiency and it can be compensated by the optimized design of the motor.

Fig. 21 shows the voltage and current waveforms when the compressor operates at 3000 and 5000 r/min. The waveforms from top to bottom are the dc-link voltage, the magnitude of the voltage vector, and the d- and q-axis current components, respectively. The magnitude of the voltage vector is lower than the dc-link voltage, which guarantees the stable operation of the electrolytic capacitor-less compressor drive system. The q-axis current fluctuates with the dc-link voltage. Although the tracking performance of the d–q currents is limited by the bandwidth of the current PI controllers, the inverter power of the electrolytic capacitor-less drive system can be effectively controlled. As a result, the harmonics of the grid current can satisfy the standards of EN61000-3-2, and the detailed harmonics measured by WT1600 are shown in Fig. 22. It can be seen that the harmonics are far lower than the required values of the standard.

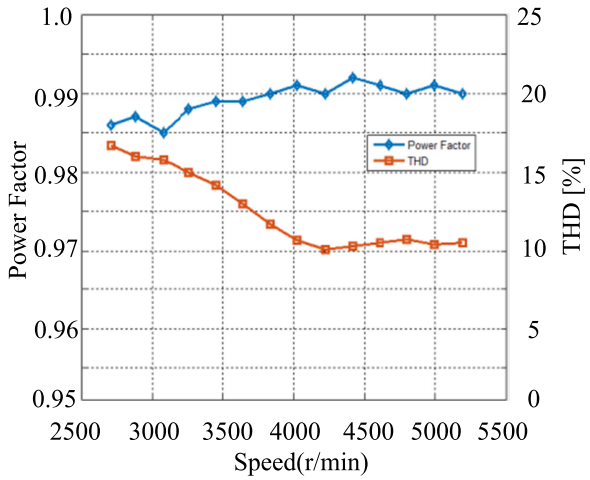

Fig. 24. Power factor and THD in the overall speed range of the compressor.

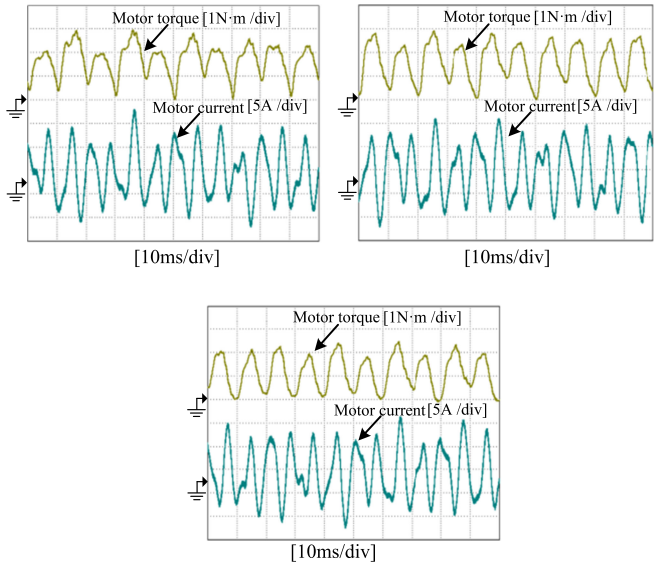

Fig. 25. Motor torque and current when the compressor operates at 3000 r/min. (a) Without inverter power control loop. (b) Only using inverter power control loop with PR controller. (c) Combining the proposed dc-link voltage regulation strategy with the inverter power control loop adopting PR controller.

Fig. 23 shows the grid voltage and current waveforms when the compressor operates at 3000 and 5000 r/min. The harmonic analysis of the current waveforms has been operated based on a longer time interval. It can be seen that the grid current is approximate to be the sinusoidal waveform and the harmonics within entire frequency range can greatly satisfy the standards of EN61000-3-2. The experimental results of the power factor and the THD at different operating speeds are shown in Fig. 24. The proposed inverter power control method can effectively maintain high power factor and low THD in the wide speed range. The maximum power factor is 0.992. The harmonics can satisfy EN61000-3-2 and the minimum THD is 10.2%. The performance of the electrolytic capacitor-less drive system can meet the requirement of the air conditioner applications. It benefits the cost reduction and reliability improvement of the system by using the proposed control method.

The motor torque in the drive system is determined by three factors: the load torque, the fluctuated dc-link voltage, and the proposed inverter power control strategy. The load torque is shown in Fig. 17, which has a large variation per mechanical cycle because of the operation principle of single rotary compressor. Hence, the motor torque will fluctuate even in normal drive strategy. The motor torque is difficult to totally track the fluctuating load torque because of the limited current bandwidth to maintain the system stable. Meanwhile, the fluctuated dc-link voltage also has an effect on the motor torque, which will be combined with the effect of load torque. The motor torque is shown in Fig. 25 (a) when the compressor operates at 3000 r/min without the proposed inverter power control loop. It can be seen that the motor torque obviously fluctuates with 100 Hz that is twice of the grid frequency and the amplitudes per cycle are various because of the periodic load torque. The motor torque only with inverter power control loop adopting PR controller and combined with dc-link voltage regulation method are shown in Fig. 25 (b) and (c), respectively. It can be seen that the motor torque in Fig. 25(b) can be easily distinguished from Fig. 25(a) because of the applied inverter power control loop. The difference among amplitudes of the torque fluctuation per cycle in Fig. 25(b) becomes less for the applied inverter power control loop. The difference of motor torque between Fig. 25(b) and (c) is not obvious, because the voltage modification vector generated by the dc-link voltage regulation has a limited effect on the motor current, which also slightly affects the motor torque. The average inverter power control performance corresponded to Fig. 25(c) is better than that in Fig. 25(b) for the better grid side quality.

V. Conclusion

This paper proposes an inverter power control strategy based on the dc-link voltage regulation applied in the electrolytic capacitor-less drive system for IPMSM. For the reduced capacity of the dc-link capacitor and the elimination of the PFC circuit, the inverter power closely affects the power factor and the THD of the grid side. The inverter power control loop with PR controller is established to regulate the inverter power, which can achieve a high gain at the fluctuation frequency of the dc-link voltage. Besides, the parameters of PR controller are easy to design. Only applying the inverter power control loop, the actual inverter power is difficult to totally track the inverter power reference because of the low bandwidth of the PI current controllers and the power coupled within the d–q reference frame. Therefore, a power compensation method based on the dc-link voltage regulation is applied to diminish the inverter power error, which does not depend on the precise calculation and is easy to realize. By using the proposed inverter power control strategy based on the dc-link voltage regulation, the power factor of the drive system can reach 0.992, and the THD of the grid current can greatly satisfy the regulations of the EN61000-3-2 without the PFC circuit. The effectiveness of the proposed method is verified on an air conditioner.

REFERENCES

[1] Z. Tang, X. Li, S. Dusmez, and B. Akin, "A new V/f based sensorless MTPA control for IPMSM drives," *IEEE Trans. Power Electron.*, vol. 31, no. 6, pp. 4400–4415, Jun. 2016.

[2] X. Lu, K. L. V. Iyer, K. Mukherjee, K. Ramkumar, and N. C. Kar, "Investigation of permanent-magnet motor drives incorporating damper bars for electrified vehicles," *IEEE Trans. Ind. Electron.*, vol. 62, no. 5, pp. 3234–3244, May 2015.

[3] M. Gu, S. Ogasawara, and M. Takemoto, "Novel PWM schemes with multi SVPWM of sensorless IPMSM drives for reducing current ripple," *IEEE Trans. Power Electron.*, vol. 31, no. 9, pp. 6461–6475, Sep. 2016.

[4] G. Zhang, G. Wang, D. Xu, and N. Zhao, "ADALINE-network-based PLL for position sensorless interior permanent magnet synchronous motor drives," *IEEE Trans. Power Electron.*, vol. 31, no. 2, pp. 1450–1460, Feb. 2016.

[5] S. Y. Jung, C. C. Mi, and K. Nam, "Torque control of IPMSM in the field-weakening region with improved dc-link voltage utilization," *IEEE Trans. Ind. Electron.*, vol. 62, no. 6, pp. 3380–3387, Jun. 2015.

[6] T. Sun, J. Wang, and X. Chen, "Maximum torque per ampere (MTPA) control for interior permanent magnet synchronous machine drives based on virtual signal injection," *IEEE Trans. Power Electron.*, vol. 30, no. 9, pp. 5036–5045, Sep. 2015.

[7] J. Y. Lee, "An EL capacitorless EV on-board charger using harmonic modulation technique," *IEEE Trans. Ind. Electron.*, vol. 61, no. 4, pp. 1784–1787, Apr. 2014.

[8] J. C. W. Lam and P. K. Jain, "A high power factor, electrolytic capacitorless AC-input LED driver topology with high frequency pulsating output current," *IEEE Trans. Power Electron.*, vol. 30, no. 2, pp. 943–955, Feb. 2015.

[9] Y. Yang, X. Ruan, L. Zhang, J. He, and Z. Ye, "Feed-forward scheme for an electrolytic capacitor-less AC/DC LED driver to reduce output current ripple," *IEEE Trans. Power Electron.*, vol. 29, no. 10, pp. 5508–5517, Oct. 2014.

[10] Y. Shi, R. Li, Y. Xue, and H. Li, "High-frequency-link-based grid-tied PV system with small DC-link capacitor and low-frequency ripple-free maximum power point tracking," *IEEE Trans. Power Electron.*, vol. 31, no. 1, pp. 328–339, Jan. 2016.

[11] G. Farivar, B. Hredzak, and V. G. Agelidis, "Reduced-capacitance thin-film H-bridge multilevel STATCOM control utilizing an analytic filtering scheme," *IEEE Trans. Ind. Electron.*, vol. 62, no. 10, pp. 6457–6468, Oct. 2015.

[12] P. Alemi, Y. C. Jeung, and D. C. Lee, "DC-link capacitance minimization in T-type three-level AC/DC/AC PWM converters," *IEEE Trans. Ind. Electron.*, vol. 62, no. 3, pp. 1382–1391, Mar. 2015.

[13] S. Harb, M. Mirjafari, and R. S. Balog, "Ripple-port module-integrated inverter for grid-connected PV applications," *IEEE Trans. Ind. Appl.*, vol. 49, no. 6, pp. 2692–2698, Nov./Dec. 2013.

[14] D. Camponogara, G. F. Ferreira, A. Campos, M. A. Dalla Costa, and J. Garcia, "Offline LED driver for street lighting with an optimized cascade structure," *IEEE Trans. Ind. Appl.*, vol. 49, no. 6, pp. 2437–2443, Nov./Dec. 2013.

[15] S. W. Kang, S. I. Kim, R. Y. Kim, and D. S. Hyun, "High power factor control of an inverter-controlled synchronous motor drive system with small DC-link capacitor," in *Proc. IEEE 39th Annu. Conf. Ind. Electron. Soc.*, 2013, pp. 7769–7774.

[16] A. Dianov, N. Kim, Y. Kim, and S. Lim, "Substitution of the universal motor drives with electrolytic capacitorless PMSM drives in home appliances," in *Proc. 9th Int. Conf. Power Electron. ECCE Asia*, Seoul, South Korea, 2015, pp. 1631–1637.

[17] W. J. Lee and S. K. Sul, "DC-link voltage stabilization for reduced DC-link capacitor inverter," *IEEE Trans. Ind. Appl.*, vol. 50, no. 1, pp. 404–414, Jan./Feb. 2014.

[18] P. Magne, D. Marx, B. Nahid-Mobarakeh, and S. Pierfederici, "Large-signal stabilization of a DC-link supplying a constant power load using a virtual capacitor: Impact on the domain of attraction," *IEEE Trans. Ind. Appl.*, vol. 48, no. 3, pp. 878–887, May/Jun. 2012.

[19] A. Yoo, S. K. Sul, S. Kim, and K. S. Kim, "Flux weakening strategy of an induction machine driven by an electrolytic capacitor-less inverter," in *Proc. Energy Convers. Congr. Expo.*, San Jose, CA, USA, 2009, pp. 147–154.

[20] D. C. Lee and Y. S. Kim, "Control of single-phase-to-three-phase AC/DC/AC PWM converters for induction motor drives," *IEEE Trans. Ind. Electron.*, vol. 54, no. 2, pp. 797–804, Apr. 2007.

[21] M. Hinkkanen and J. Luomi, "Induction motor drives equipped with diode rectifier and small DC-link capacitance," *IEEE Trans. Ind. Electron.*, vol. 55, no. 1, pp. 312–320, Jan. 2008.

[22] S. Kim and J. K. Seok, "Induction motor control with a small DC-link capacitor inverter fed by three-phase diode front-end rectifiers," *IEEE Trans. Power Electron.*, vol. 30, no. 5, pp. 2713–2720, May 2015.

[23] H. Yoo and S. K. Sul, "A novel approach to reduce line harmonic current for a three-phase diode rectifier-fed electrolytic capacitor-less inverter," in *Proc. IEEE 24th Annu. Appl. Power Electron. Conf. Expo.*, Washington, DC, USA, 2009, pp. 1897–1903.

[24] Y. Zhou, W. Huang, and F. Hong, "Single-phase input variable-speed AC motor system based on electrolytic capacitor-less single-stage boost three-phase inverter," *IEEE Trans. Power Electron.*, vol. 31, no. 10, pp. 7043–7052, Oct. 2016.

[25] H. Shin, Y. Son, Y. H. Chae, and J. I. Ha, "Single-phase grid connected motor drive system with DC-link shunt compensator and small DC-link capacitor," *IEEE Trans. Power Electron.*, vol. 32, no. 2, pp. 1268–1278, Feb. 2017.

[26] S. Xuan, Q. Gao, Y. Wang, X. Cai, and L. Luo, "An electrolytic capacitor-less IPMSM drive with input current shaping based on the predictive control," in *Proc. 17th Eur. Conf. Power Electron. Appl.*, Geneva, Switzerland, 2015, pp. 1–7.

[27] I. Takahashi and H. Haga, "Direct torque IPM motor control method to obtain unity power factor using a single-phase diode rectifier," in *Proc. IEEE. Int. Elect. Mach. Drives Conf.*, Jun. 2003, vol. 2, pp. 1078–1083.

[28] H. Lamsahel and P. Mutschler, "Permanent magnet drives with reduced DC-link capacitor for home appliances," in *Proc. IEEE 35th Annu. Conf. Ind. Electron.*, 2009, pp. 725–730.

[29] H. S. Jung, S. J. Chee, S. K. Sul, Y. J. Park, H. S. Park, and W. K. Kim, "Control of three-phase inverter for AC motor drive with small DC-link capacitor fed by single-phase AC source," *IEEE Trans. Ind. Appl.*, vol. 50, no. 2, pp. 1074–1081, Mar./Apr. 2014.

[30] K. Inazuma, H. Utsugi, K. Ohishi, and H. Haga, "High power factor single-phase diode rectifier driven by repetitively controlled IPM motor," *IEEE Trans. Ind. Electron.*, vol. 60, no. 10, pp. 4427–4437, Oct. 2013.

[31] Y. Son and J. I. Ha, "Direct power control of three phase inverter for grid input current shaping of single phase diode rectifier with small DC-link capacitor," *IEEE Trans. Power Electron.*, vol. 30, no. 7, pp. 3794–3803, Jul. 2015.

[32] A. Kuperman, "Proportional-resonant current controllers design based on desired transient performance," *IEEE Trans. Power Electron.*, vol. 30, no. 10, pp. 5341–5345, Oct. 2015.

[33] D. G. Holmes, T. A. Lipo, B. P. McGrath, and W. Y. Kong, "Optimized design of stationary frame three phase AC current regulators," *IEEE Trans. Power Electron.*, vol. 24, no. 11, pp. 2417–2426, Nov. 2009.

[34] T. Ye, N. Dai, C. Lam, M. Wong, and J. Guerrero, "Analysis, design and implementation of a quasi-proportional-resonant controller for a multi-functional capacitive-coupling grid-connected inverter," *IEEE Trans. Ind. Appl.*, vol. 52, no. 5, pp. 4269–4280, Sep./Oct. 2016.

Nannan Zhao received the B.S. and M.S. degrees in control science and engineering from Harbin Institute of Technology, Harbin, China, in 2013 and 2015, respectively, where he is currently working toward the Ph.D. degree in power electronics and electrical drives in the School of Electrical Engineering and Automation.

His current research interests include advanced control of permanent magnet synchronous motor drives and position sensor-less control of AC motors.

Gaolin Wang (M'13) received the B.S., M.S., and Ph.D. degrees in electrical engineering from Harbin Institute of Technology, Harbin, China, in 2002, 2004, and 2008, respectively.

In 2009, he joined the Department of Electrical Engineering, Harbin Institute of Technology as a Lecturer, where he has been a Professor of electrical engineering since 2014. From 2009 to 2012, he was a Postdoctoral Fellow in Shanghai STEP Corporation. He has authored more than 50 technical papers published in journals and conference proceedings. He has ten Chinese patents. His current major research interests include permanent magnet synchronous motor drives, high performance direct-drive for traction system, position sensorless control of AC motors, and efficiency optimization control of interior PMSM.

Dianguo Xu (M'97–SM'12–F' 16) received the B.S. degree in control engineering from Harbin Engineering University, Harbin, China, in 1982, and the M.S. and Ph.D. degrees in electrical engineering from Harbin Institute of Technology (HIT), Harbin, China, in 1984 and 1989, respectively.

In 1984, he joined the Department of Electrical Engineering, HIT, as an Assistant Professor. Since 1994, he has been a Professor in the Department of Electrical Engineering, HIT. From 2000 to 2010, he was the Dean of the School of Electrical Engineering and Automation, HIT. He is currently the Vice President of HIT. His research interests include renewable energy generation technology, power quality mitigation, sensorless vector controlled motor drives, and high performance servo system. He has published more than 600 technical papers.

Dr. Xu is an Associate Editor of the IEEE TRANSACTIONS ON INDUSTRIAL ELECTRONICS and the IEEE JOURNAL OF EMERGING AND SELECTED TOPICS IN POWER ELECTRONICS. He serves as the Chairman of IEEE Harbin Section.

Lianghong Zhu received the B.S. degree in mechanical manufacture technology and equipment from Hefei University of Technology, Hefei, China, in 2001, and the M.S. degree in measuring and testing technologies and instruments from Huaqiao University, Quanzhou, China, in 2004.

In 2005, he joined the R and D Center of Residential Air-Conditioning Division, Midea Group, engaged in air-conditioning inverter controller design and application development. He has authored ten technical papers published in journals. He has applied for more than 60 patents, of which 5 invention patents and 20 utility model patents have been authorized.

Mr. Zhu received the second prize of China National Science and Technology Progress Award in 2014.

Guozhu Zhang received the B.S. degree in automation and the Ph.D. degree in control science and engineering from Beijing Institute of Technology, Beijing, China, in 2005 and 2010, respectively.

In 2010, he joined the R and D Center of Residential Air-Conditioning Division, Midea Group, where he has been a Senior Research Engineer since 2014. He has authored more than 20 technical papers published in journals and conference proceedings. He is the holder of five Chinese patents. His current major research interests include permanent magnet synchronous motor drives, power factor correction, and compressor control.

Junya Huo received the B.S. degree in mechanical design manufacture and automation and the M.S. degree in mechanical and electronic engineering from Central South University, Changsha, China, in 2003 and 2006, respectively.

In 2006, he joined the R and D Center of Residential Air-Conditioning Division, Midea Group, where he has been an Associate Senior Engineer of Light Industrial Refrigeration Equipment Engineering since 2014. He has authored more than seven technical papers published in journals and conference proceedings. He is the holder of 13 Chinese patents. His current major research interests include permanent magnet synchronous motor drives and compressor control.